

A spectral stacking analysis to search for faint outflow signatures in $z \sim 6$ quasars

F. Stanley, J. B. Jolly, S. König and K. K. Knudsen

Department of Space, Earth and Environment, Chalmers University of Technology, Onsala Space Observatory, SE-439 92 Onsala, Sweden
e-mail: flora.stanley@chalmers.se

Accepted August 2019

ABSTRACT

Aims. Outflows in quasars during the early epochs of galaxy evolution are an important part of the feedback mechanisms potentially affecting the evolution of the host galaxy. However, systematic observations of outflows are only now becoming possible with the advent of sensitive mm telescopes. In this study we use spectral stacking methods to search for faint high velocity outflow signal in a sample of [C II] detected, $z \sim 6$ quasars.

Methods. We search for broad emission line signatures from high-velocity outflows for a sample of 26 $z \sim 6$ quasars observed with the Atacama Large Millimeter Array (ALMA), with a detection of the [C II] line. The observed emission lines of the sources are dominated by the host galaxy, and outflow emission is not detected for the individual sources. We use a spectral line stacking analysis developed for interferometric data to search for outflow emission. We stack both extracted spectra and the full spectral cubes. We also investigate the possibility that only a sub-set of our sample contributes to the stacked outflow emission.

Results. We find only a tentative detection of a broad emission line component in the stacked spectra. When taking a region of about $2''$ around the source central position of the stacked cubes, the stacked line shows an excess emission due to a broad component of $1.1\text{--}1.5\sigma$, but the significance drops to $0.4\text{--}0.7\sigma$ when stacking the extracted spectra from a smaller region. The broad component can be characterised by a line width of full width half-max FWHM $> 700 \text{ km s}^{-1}$. Furthermore, we find a sub-sample of 12 sources the stack of which maximises the broad component emission. The stack of this sub-sample shows an excess emission due to a broad component of $1.2\text{--}2.5\sigma$. The stacked line of these sources has a broad component of FWHM $> 775 \text{ km s}^{-1}$.

Conclusions. We find evidence suggesting the presence of outflows in a sub-sample of 12 out of 26 sources, and have demonstrated the importance of spectral stacking techniques in tracing faint signal in galaxy samples. However, deeper ALMA observations are necessary to confirm the presence of a broad component in the individual spectra.

Key words. galaxy evolution – galaxies: quasars – submillimeter: galaxies – galaxies: high-redshift

1. Introduction

Our understanding of redshift $z \gtrsim 6$ galaxies and super-massive black holes (SMBHs) has increased significantly, and still continues to do so. More and more quasars are detected at high redshifts, with their numbers now in the hundreds at redshifts $z > 5.5$ (e.g., Bañados et al. 2016; Jiang et al. 2016). These quasars are known to have BH masses of $> 10^9 M_{\odot}$ (e.g., Fan et al. 2006; Kurk et al. 2007; De Rosa et al. 2011). Their hosts tend to be massive galaxies with stellar masses of $10^{10} - 10^{11} M_{\odot}$. Star formation rates (SFRs) in $z \sim 6$ quasar host galaxies can range between $10\text{--}3000 M_{\odot} \text{ yr}^{-1}$ (e.g., Omont et al. 2013; Willott et al. 2013; Venemans et al. 2012, 2016; Wang et al. 2016; Willott et al. 2017; Venemans et al. 2018), and they appear gas and dust-rich (e.g., Maiolino et al. 2005; Wang et al. 2011, 2013; Venemans et al. 2017). However, we are still lacking understanding of if and how quasar feedback affects the host galaxy and the surrounding environment.

Massive outflows observed in active galaxies are linked with the feedback that regulates the overall star formation and BH growth (e.g., Fabian 2012; King & Pounds 2015). Observational studies of local and low-redshift galaxies have yielded a large number of outflow detections, both in the ionized and the molecular gas phases, that are seen in starburst galaxies as well as active galactic nuclei (AGN, e.g., Rupke & Veilleux 2011; Sturm

et al. 2011; Maiolino et al. 2012; Veilleux et al. 2013; Cicone et al. 2014; Harrison et al. 2014; Tadhunter et al. 2018; Barcos-Muñoz et al. 2018; Gallerani et al. 2018, see also review by Fabian 2012). Furthermore, simulations of galaxy formation and evolution find that feedback is necessary in order to reproduce the observed galaxy stellar mass functions (e.g., Somerville et al. 2008; Sijacki et al. 2015; Schaye et al. 2015). Therefore, it is necessary to characterise the physical properties of quasar outflows observationally, as well as from simulations, to constrain their feedback mechanisms.

As the cosmic SFR peaks only a few billion years after the Big Bang, the detection and characterisation of outflows in the high redshift quasar populations is a necessity if we are to understand early galaxy evolution. For high-redshift galaxies, the number of detections is still limited, in part because of the large distances resulting in the faintness of the sources, and the limited spatial resolution. Currently, only a single detection of a [C II] outflow is known in a quasar at redshift $z \sim 6$ - SDSS J1148+5251 (e.g., Maiolino et al. 2012; Cicone et al. 2015). However, recent mm observations of $z > 5$ quasars (e.g. Venemans et al. 2016, 2017; Venemans 2017; Willott et al. 2017; Decarli et al. 2017, 2018) and star-forming galaxy samples (e.g. Gallerani et al. 2018) have allowed for the search of outflow signatures in more sources. In a study of 27 quasars at $z \sim 6$, Decarli

arXiv:1908.11395v1 [astro-ph.GA] 29 Aug 2019

et al. (2018) found a high detection rate of 85% in [C II], in contrast to normal star-forming galaxies (e.g., Knudsen et al. 2016). Finding no evidence of outflows in the individual sources, Decarli et al. (2018) examined the possibility of an outflow signature in the stacked spectra of the full sample. The stacked spectra showed no evidence of an outflow component; however, the authors only took into account the signal within the central pixel of each target. Interestingly, a study of 9 star-forming galaxies at similar redshifts of $z \sim 5.5$ observed in [C II] shows excess emission in their stacked spectra at high velocities (~ 1000 km/s) that could be attributed to the presence of outflows (Gallerani et al. 2018).

In this study we aim to use recent ALMA archival data to examine the presence of outflows in a sample of $z \sim 6$ quasars observed in [C II]. Using extensive spectral stacking analysis over the extended galaxy regions, we examine the presence of an outflow component in the stacked [C II] line, over a larger area. Furthermore, we use sub-sampling to determine a sub-sample of sources most likely to have an outflow component when stacked. We note that this paper was written in parallel to the recent article by Bischetti et al. (2019) with a similar aim to our work. However, our sample selection, redshift range, and analysis are different.

In Sect. 2 we present the sample of quasars selected from the ALMA archive along with a description of the projects they come from. In Sect. 3 we describe the data reduction and analysis. In Sect. 4 we present methods used in our stacking analysis. The results are given in Sect. 5, followed by the discussion in Sect. 6. Finally, in Sect. 7 we give a brief summary and the conclusions of this work. Throughout this paper we assume $H_0 = 70 \text{ km s}^{-1} \text{ Mpc}^{-1}$, $\Omega_M = 0.3$, $\Omega_\Lambda = 0.7$.

2. Sample

To study the outflow activity in distant quasars, we selected sources at $z \sim 6$ that have been observed with ALMA in the far-infrared fine-structure line [C II] $^2\text{P}_{3/2}-^2\text{P}_{1/2}$, at a rest frequency of 1900.537 GHz ($\lambda \sim 158 \mu\text{m}$). The sample was selected from the ALMA archive from relatively recent cycles (observing cycle 3 and above) to ensure that all sources were observed with similar technical specifications, such as the number of antennas and uv -coverage. Additionally, the sample was limited to the sources for which the data was public by January 2018.

Our sample consists of 32 optically-selected quasars (see Table 1) from projects *2015.1.00606.S* (Willott et al. 2017), *2015.1.00997.S* (PI: R. Maiolino), and *2015.1.01115.S* (Decarli et al. 2018). The sample has redshifts of $5.779 < z < 6.661$, and absolute magnitudes at 1450 \AA of $-27.8 < M_{1450 \text{ \AA}} < -23.89$ that correspond to bolometric luminosities of $3.9 \times 10^{45} < L_{\text{bol}} < 10^{47} \text{ erg s}^{-1}$ (converted following Runnoe et al. 2012; Venemans et al. 2016, see table 1). In Fig. 1 we show the distribution of the L_{bol} together with the distribution of the redshift, for a total of 321 quasars from (Bañados et al. 2016, and references therein), Jiang et al. (2016), and Mazzucchelli et al. (2017). The sample of quasars used in our analysis are overplotted as red triangles. Our sample covers the majority of the bolometric luminosity range of the general detected population, while concentrating on the higher end of the redshift distribution by design. Therefore, it is representative of optically selected quasars at redshifts of $z = 5.8 - 6.7$.

As the purpose of this study is to determine the presence of an outflow component, we only include the sample sources where the [C II] line was detected. As a result, we find that 26 sources are detected, and the data are of sufficient quality to be

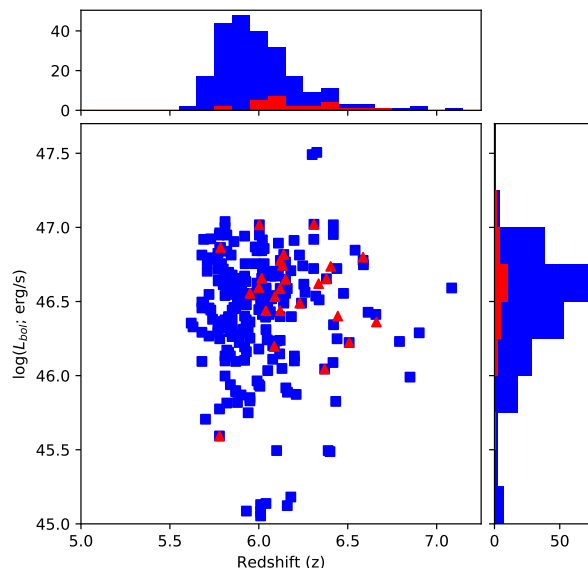


Fig. 1: The AGN bolometric luminosity (L_{bol}) as a function of redshift (z) of our sample (red triangles). Also plotted are the known high redshift quasars from the compiled catalogue of Bañados et al. (2016), the catalogue of SDSS detections of Jiang et al. (2016) and the new detections of Mazzucchelli et al. (2017), from which the majority of our sample has been selected.

used for the purpose of this paper. This final sample is provided in Table 2.

3. ALMA data reduction and analysis

After extracting the [C II] raw data of the 31 quasars from the ALMA archive, we calibrated and imaged (including continuum subtraction) each data set with the Common Astronomy Software Applications¹. For about 70% of the sources, a careful manual calibration of the observations was necessary to warrant that the data were calibrated correctly. This was necessary in order to address issues found with flux calibration², incorrect antenna positions³, low source amplitudes requiring additional flagging, and other issues found in the original calibration. Specifically for the sources with flux calibration issues we found that the fluxes were wrong by $\sim 20-45\%$. For the remaining $\sim 30\%$ of the sources, the calibration results from the ALMA pipeline were sufficient. For the manually calibrated data sets, we used the CASA software version 5.1.1, to ensure that bugs and calibration issues found for previous CASA versions have

¹ <http://casa.nrao.edu/> (CASA, McMullin et al. 2007)

² This is the case for sources originally calibrated with CASA version 4.6 or prior with the sources Ceres or Pallas as their flux calibrators. Through private communication with the ALMA Nordic ARCnode it was pointed out to us that for those versions of CASA the flux models for Pallas and Ceres were wrong. Consequently, the fluxes extrapolated for the sources observed with Ceres or Pallas as flux calibrators will be wrong without re-calibration.

³ In these cases the data were observed right after a shift in the antenna positions but did not have the new correct coordinates when original calibration was performed. We have made sure to use the correct coordinates.

Table 1: Properties for our sample of $z \sim 6$ quasars available in the ALMA archive by January 2018. (a) The identification (ID) of the source, with the associated numbers corresponding to the references of the source (including Bischetti et al. 2019; Decarli et al. 2018; Willott et al. 2017, in which the ALMA data have been published); (b) & (c) the J2000 RA & DEC coordinates of the sources from the optical; (d) redshift of source in the literature; (e) the bolometric AGN luminosity estimated from the 1450Å absolute magnitudes found in the literature; (f) The ProjectID of the ALMA project the source was observed in, where A=2015.1.00606.S, B=2015.1.00997.S, C=2015.1.01115.S; (g) flag on whether or not we detect the [CII] line in our analysis, (h) The original beamsizes of the natural weighted images, before re-imaging to a $0.8'' \times 0.8''$ beamsizes.

ID ^(a)	RA ^(b) hh:mm:ss	DEC ^(c) dd:mm:ss	z ^(d)	$\log L_{\text{bol}}$ ^(e)	Project ^(f)	[CII] ^(g) detected	Original ^(h) beamsize
PSO J007.0273+04.9571 ^{1,2,6}	00:28:06.56	+04:57:25.7	6.00	46.59	C	Y	$0.65'' \times 0.47''$
PSO J009.7355-10.4316 ^{2,6}	00:38:56.52	-10:25:53.9	5.95	46.55	C	Y	$0.63'' \times 0.44''$
SDSS J0129-0035 ^{3,16}	01:29:58.51	-00:35:39.7	5.779	45.59	B	Y	$0.45'' \times 0.38''$
VST-ATLAS J025.6821-33.4627 ^{2,4,6} (J0142-3327)	01:42:43.73	-33:27:45.5	6.31	47.02	C	Y	$0.87'' \times 0.75''$
PSO J065.4085-26.9543 ^{2,6}	04:21:38.05	-26:57:15.6	6.14	46.82	C	Y	$1.11'' \times 0.83''$
PSO J065.5041-19.4579 ^{2,6}	04:22:00.99	-19:27:28.7	6.12	46.59	C	Y	$1.09'' \times 0.75''$
VDESJ0454-4448 ^{2,6,13}	04:54:01.79	-44:48:31.1	6.09	46.53	C	Y	$1.12'' \times 0.79''$
SDSS J0842+1218 ^{2,5,6,8}	08:42:29.23	+12:18:48.2	6.069	46.69	C	N*	$1.26'' \times 1.12''$
PSO J159.2257-02.5438 ^{2,6}	10:36:54.19	-02:32:37.9	6.38	46.65	C	Y	$1.28'' \times 0.98''$
SDSS J1030+0524 ^{2,6}	10:30:27.10	+05:24:55.0	6.308	46.72	C	N	$1.21'' \times 0.98''$
SDSS J1044-0125 ^{2,3}	10:44:33.04	-01:25:02.2	5.7847	46.86	B	Y	$0.74'' \times 0.70''$
VIK J1048-0109 ^{6,15}	10:48:19.09	-01:09:40.3	6.661	46.36	C	Y	$1.46'' \times 1.00''$
PSO J167.6415-13.4960 ^{2,6,14,19}	11:10:33.98	-13:29:45.6	6.508	46.22	A,C	Y	$0.77'' \times 0.63''$
ULAS J1148+0702 ^{2,6}	11:48:03.29	+07:02:08.3	6.32	46.54	C	N	$1.32'' \times 1.08''$
VIK J1152+0055 ^{2,6,10}	11:52:21.27	+00:55:36.7	6.37	46.04	C	Y	$1.26'' \times 1.02''$
ULAS J1207+0630 ^{2,6}	12:07:37.44	+06:30:10.4	6.04	46.59	C	N*	$1.73'' \times 0.89''$
PSO J183.1124+05.0926 ^{2,6}	12:12:26.98	+05:05:33.5	6.4039	46.73	C	Y	$1.25'' \times 1.05''$
SDSS J1306+0356 ^{2,6,7}	13:06:08.26	+03:56:26.3	6.016	46.66	C	Y	$1.11'' \times 0.90''$
ULAS J1319+0950 ^{2,6,12}	13:19:11.29	+09:50:51.4	6.133	46.74	B	Y	$1.20'' \times 1.04''$
PSO J217.0891-16.0453 ^{2,6}	14:28:21.39	-16:02:43.3	6.11	46.70	C	N*	$1.17'' \times 0.86''$
CFHQS J1509-1749 ^{2,6,17}	15:09:41.78	-17:49:26.8	6.121	46.78	C	Y	$1.36'' \times 0.87''$
PSO J231.6576-20.8333 ^{5,6,11}	15:26:37.84	-20:50:00.7	6.586	46.80	C	Y	$1.21'' \times 0.88''$
PSO J308.0416-21.2339 ^{2,5,6}	20:32:09.99	-21:14:02.3	6.23	46.49	C	Y	$0.85'' \times 0.65''$
SDSS J2054-0005 ^{2,3}	20:54:06.49	-00:05:06.49	6.0391	46.44	B	Y	$0.69'' \times 0.67''$
CFHQS J2100-1715 ^{2,5,6,18}	21:00:54.62	-17:15:22.5	6.087	46.20	C	Y	$0.73'' \times 0.63''$
VIK J2211-3206 ^{6,15}	22:11:12.39	-32:06:12.9	6.336	46.62	C	Y	$0.84'' \times 0.67''$
VIMOS2911001793 ^{6,19}	22:19:17.22	+01:02:48.90	6.16	(-22.60)	A	Y	$0.77'' \times 0.68''$
PSO J340.2041-18.6621 ^{2,6}	22:40:49.00	-18:39:43.8	6.01	46.51	C	N	$0.78'' \times 0.68''$
SDSS J2310+1855 ^{2,3,9}	23:10:38.88	+18:55:19.7	6.0031	47.02	B	Y	$1.10'' \times 0.73''$
VIK J2318-3113 ¹⁵	23:18:18.35	-31:13:46.4	6.444	46.40	C	Y	$0.82'' \times 0.78''$
VIK J2318-3029 ¹⁵	23:18:33.10	-30:29:33.4	6.12	46.44	C	Y	$0.91'' \times 0.74''$
PSO J359.1352-063831 ^{2,6}	23:56:32.00	-06:22:59.0	6.15	46.65	C	Y	$1.06'' \times 0.62''$

References: 1: Bañados et al. (2014); 2: Bañados et al. (2016); 3: Bischetti et al. (2019); 4: Carnall et al. (2015); 5: Decarli et al. (2017); 6: Decarli et al. (2018); 7: Fan et al. (2001); 8: Jiang et al. (2015); 9: Jiang et al. (2016); 10: Matsuoka et al. (2016); 11: Mazzucchelli et al. (2017); 12: Mortlock et al. (2009); 13: Reed et al. (2015); 14: Venemans et al. (2015); 15: Venemans et al. (in prep.); 16: Wang et al. (2013); 17: Willott et al. (2007); 18: Willott et al. (2010); 19: Willott et al. (2017). *These sources are not detected in our analysis; however if only the central pixel of the source is taken the [CII] line is detected in agreement with Decarli et al. (2018).

been corrected for. Hereafter, a few details are given for each of the archival ALMA projects:

2015.1.00606.S: As part of the work presented here, two sources of this program were extracted from the ALMA archive. Observations took place on March 22, 2016, and April 27, 2016. 37 antennas were included in the array with minimum and maximum baselines of 15.3 m and 460.0 m, respectively. Applying natural weighting, the resulting beam size is $0.8'' \times 0.6''$. The spectral setup consisted of four spectral windows of 2.0 GHz bandwidth, each containing 128 channels of 15.625 MHz width.

2015.1.00997.S: The five sources (see Table 1) we included

from this program have been observed between January and July 2016. Between 37 and 49 antennas were included in the arrays with baselines between 15.1 m and 1.0 km. The synthesised beam sizes resulting from natural weighting ranged between $\sim 0.4''$ and $\sim 1.2''$. The observations were setup with four spectral windows of 1.875 GHz bandwidth each, 480 channels per spectral window, and 3.9 MHz wide channels.

2015.1.01115.S: The 26 sources taken from this program were included in our sample. The data were obtained between January and June 2016 in arrays with baselines between 15.1 m and 704.1 m. Natural weighting led to synthesised beam sizes

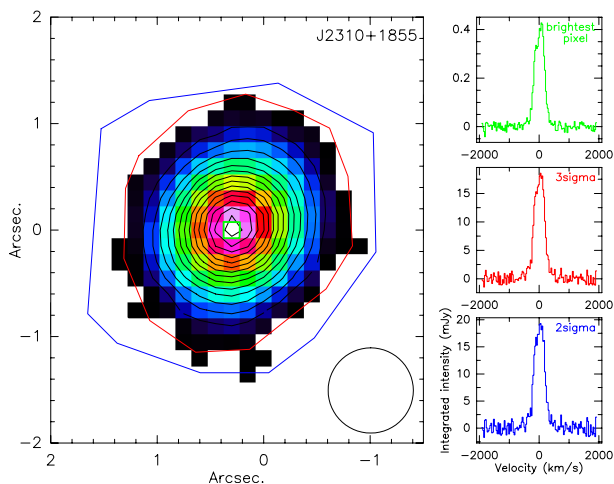


Fig. 2: Example for an integrated intensity distribution (moment zero map) and spectra extracted from different regions in J2310+1855. The green box marks the area of the brightest pixel, the area marked by the red line contains all signal above the 3σ threshold, and the blue line outlines the region with signals above 2σ . The spectra extracted from these three regions are shown on the right-hand side. They are color-coded according to the region from which they were extracted, and the region of extraction is mentioned in the panel for each spectrum as well. On the lower-left side of the image we also show the beam size of our images.

between $\sim 0.4''$ and $1.7''$. For the spectral setup, 960 channels of 1.953 MHz width covered each of the four 1.875 GHz wide spectral windows. For more extensive details see Decarli et al. (2018).

Finally, all data cubes were imaged to the same angular resolution of $0.8'' \times 0.8''$ and spectral resolution of 30 km s^{-1} , with a pixel scale of $0.2''$. Continuum subtraction was performed using the CASA task `uvcontsub`, using the channels with no line emission. The uncertainty of the absolute flux calibration for all sources falls within 5–10%. For further spectral analysis, the resulting data cubes were imported into the MAPPING software package within GILDAS⁴. From the continuum-subtracted cubes, we created integrated intensity maps (moment-0) of the [C II] line for each source. With the help of these maps we extracted 1-D spectra from the position of the brightest pixel, and the individual areas enclosed by the 2 and 3σ integrated intensity contours (for an example see Fig. 2). We extracted the continuum flux densities (S_{cont}) of each source using a 2D Gaussian fit to the continuum source. The IR ($8\text{--}1000\mu\text{m}$) luminosity of the sources was estimated by normalising a set of star-forming galaxy templates (from Mullaney et al. 2011, see also Stanley et al. 2018) to the measured S_{cont} values.

4. Spectral line stacking techniques

To search for outflow signatures in our sample of $z \sim 6$ quasars, we use the spectral stacking analysis tool `LINE STACKER` (Jolly et al. in prep). Stacking the [C II] line of the quasars in our sample will allow us to search for a broad emission line component, that is weak in comparison to the bright [C II] main line component, and is typically undetected in the individual spectra. We only use the sources where [C II] has been detected, as the detection

provides the redshift, and the systemic velocity of the line of each quasar host galaxy.

4.1. Velocity re-binning

To account for the range of line widths (FWHM) observed for the [C II] lines in our sample, we choose to normalise all line widths to the same value. The [C II] lines of all sources are re-binned in channel space with respect to the smallest FWHM measured in the sample, so that each [C II] FWHM is covered by the same number of channels albeit of different channel width. We chose to normalise to the narrowest line and not the widest to avoid oversampling of the data. We note that any subsamples selected use the re-binned spectra as defined for the full sample. For a [C II] line that has a larger FWHM than the narrowest line, the channels are re-defined to have a width of: $cw_{\text{rebin}} = cw_{\text{orig}} \times \text{FWHM}_{\text{orig}} / \text{FWHM}_{\text{min}}$, where cw_{rebin} is the channel width after re-binning, cw_{orig} is the original channel width of 30 km s^{-1} (see Sect. 3), and FWHM_{min} is the FWHM of the narrowest line, which corresponds to 270 km/s .

As a result of the re-binning, the outer velocity bins of the stacked spectrum are not sampled by the same number of sources as the central bins close to the [C II] line core. For the analysis we only consider the central part of the spectrum where the channels include information from the majority of the stacked sample. As we are looking at the mean stacked spectra of the sample, the channel width of the stacked spectrum is taken as the mean channel width of all the individual spectra once re-binned, for our sample that corresponds to 60 km s^{-1} .

4.2. 1-D and 3-D stacking

In our analysis we perform both 1-D and 3-D stacking. For the 1-D stacking, we first extract the integrated spectrum for each source, from the region where the moment zero maps have a $> 2\sigma$ emission. We then re-bin the spectra as described in Sect. 4.1, and stack. For the 3-D stacking, we take the full spectral cubes of each source. Following the method described in Sect. 4.1 we re-bin the full cube using the same parameters determined in our 1-D analysis. The cubes are then stacked pixel by pixel in order to create the stacked cube. The stacked cube allows us to extract the stacked spectrum from different regions as well as image different parts of the stacked spectrum.

4.3. Weighting schemes for the line stacking

In our stacking analysis we use 3 different types of weights when stacking the spectra:

- $w = 1$, i.e., no weighting.
- $w = 1/\sigma_{\text{rms}}^2$, i.e., weighting by the noise. In this case, the weight is applied in each velocity channel of the re-binned spectra, using the corresponding noise in that channel. Like this, we take the variations in noise levels of the different observations and spectral channels into account. This is important, as we are interested in the relatively weak outflow component.
- $w = 1/S_{\text{peak}}$, i.e., weighting by the peak flux of the detected [C II] line (S_{peak}). With these weights, we normalise for the varying strength of the main component, so that bright lines do not dominate the result.

⁴ <http://www.iram.fr/IRAMFR/GILDAS>

Table 2: Results of the observations for the sample sources. We note that only sources with a [C II] detection are included here (see Table 1). (a) Source ID; (b) Observed [C II] frequency; (c) [C II] redshift calculated from the observed line; (d) the rms of the spectrum from the final imaging with beamsize of $0.8'' \times 0.8''$, and channelwidths of 30 km/s; (e) the peak flux density of the [C II] line; (f) the band-6 continuum flux density; (g) the IR (8–1000 μ m) luminosity calculated from the band-6 continuum. In bold we highlight the sources included in the *max sub-sample*.

ID ^(a)	[CII] freq. ^(b) [GHz]	$z_{\text{[CII]}}$ ^(c)	rms ^(d) [mJy/beam]	$S_{\text{peak}}^{\text{(e)}}$ [mJy]	FWHM [km/s]	$S_{\text{cont}}^{\text{(f)}}$ [mJy]	$L_{\text{IR}}^{\text{(g)}}$ [$10^{12}L_{\odot}$]
PSO J007.0273+04.9571	271.463	6.001	0.39	4.89	965	1.87 ± 0.04	2.09 ± 0.48
PSO J009.7355-10.4316	271.364	6.004	0.36	17.32	583	1.60 ± 0.04	1.78 ± 0.41
SDSS J0129-0035	280.390	5.778	0.10	10.60	384	2.65 ± 0.02	2.9 ± 0.7
VST-ATLAS J025.6821–33.4627	259.010	6.338	0.70	12.16	656	1.19 ± 0.05	1.4 ± 0.3
PSO J065.4085-26.9543	264.429	6.187	0.79	7.12	854	1.00 ± 0.05	1.2 ± 0.3
PSO J065.5041-19.4579	266.753	6.125	0.73	3.47	777	0.38 ± 0.05	0.4 ± 0.1
VDESJ0454-4448	269.272	6.058	0.62	1.68	726	0.55 ± 0.04	0.6 ± 0.1
PSO J159.2257-02.5438	257.450	6.382	0.54	3.90	717	0.53 ± 0.04	0.6 ± 0.1
SDSS J1044-0125	280.106	5.786	0.24	4.16	895	3.03 ± 0.02	3.3 ± 0.8
VIK J1048-0109	247.600	6.676	0.49	7.42	707	2.50 ± 0.04	3.1 ± 0.7
PSO J167.6415-13.4960	252.932	6.514	0.21	7.97	1003	0.58 ± 0.04	0.7 ± 0.2
VIK J1152+0055	258.045	6.365	0.74	2.27	386	0.09 ± 0.03	0.1 ± 0.04
PSO J183.1124+05.0926	255.500	6.438	0.66	19.05	763	3.99 ± 0.05	5 ± 1
SDSS J1306+0356	270.181	6.034	0.76	9.46	598	0.82 ± 0.04	0.9 ± 0.2
ULAS J1319+0950	266.431	6.133	0.37	9.05	1016	4.59 ± 0.03	5 ± 1
CFQS J1509-1749	266.859	6.122	0.66	3.54	1135	1.46 ± 0.04	1.7 ± 0.4
PSO J231.6576-20.83335	250.490	6.587	0.68	8.13	922	3.34 ± 0.12	4 ± 1
PSO J308.0416-21.2339	262.616	6.237	0.56	6.20	1128	0.53 ± 0.05	6.1 ± 0.1
SDSS J2054-0005	270.007	6.039	0.33	13.81	441	2.60 ± 0.03	2.9 ± 0.7
CFQS J2100-1715	268.393	6.081	0.51	3.16	870	0.36 ± 0.05	0.4 ± 0.1
VIK J2211-3206	258.963	6.339	0.57	0.71	807	0.59 ± 0.03	0.7 ± 0.2
VIMOS2911001793	265.832	6.14	0.22	8.8	270	0.76 ± 0.03	0.86 ± 0.19
SDSS J2310+1855	271.397	6.003	0.38	19.71	788	6.97 ± 0.05	8 ± 2
VIK J2318-3113	255.329	6.443	0.84	2.96	609	0.36 ± 0.04	0.4 ± 0.1
VIK J2318-3029	265.960	6.146	0.93	7.36	582	2.33 ± 0.06	2.7 ± 0.6
PSO J359.1352-06.3831	265.007	6.172	0.84	6.53	626	0.60 ± 0.06	0.7 ± 0.2

We repeat our stacking analysis for the three different weighting schemes to search for an outflow component and determine the effects of the varying [C II] line strengths, and noise levels.

5. Results

5.1. Stacking the full sample

In the first column of Fig. 3 we show the 1-D stacked spectra for the full sample, for the three different weights used. At the bottom of the figure we also show the number of sources included in each channel. The results from fitting the stacked line are given in Table 3. Including a broad component in the fit improves the χ^2 of the fit by 24, 23, and 14% for stacks with weights of $w = 1$, $w = 1/\sigma_{\text{rms}}^2$, and $w = 1/S_{\text{peak}}$, respectively. However, the fitted parameters for the broad component are not well constrained (see Table 3).

We estimate the significance of the excess emission not accounted for by the single component fit to the line. For this we subtract the single component fit from the spectrum, and take the sum of the residuals within ± 800 km/s. We find a significance of $0.4\text{--}0.7\sigma$, depending on the weighting scheme used (see Table 5).

In Fig. 4 (*top panel*) we show the stacked cubes of the full sample for the non-weighted stacks. Also shown are the one-component (red) and two-component (blue) fits to the line. The

results of the two-component fits to the stacked line are given in Table 4. In the right of Fig. 4 we also show the collapsed image of the wing channels, covering velocities of $\pm 420 - 840$ km s $^{-1}$. In this case, including a broad component improves the χ^2 of the fit by 46%, 15%, 34% for weights of $w = 1$, $w = 1/\sigma_{\text{rms}}^2$, and $w = 1/S_{\text{peak}}$, respectively. Following the methods described earlier, we calculate the significance of the excess emission to be $1.1\text{--}1.5\sigma$, depending on the weighting scheme used (see Table 5).

The 3-D stacked line differs to that from our 1-D stacking analysis. This is due to the fact that in our 3-D stacking analysis we use a larger integration area ($2''$) than that used in the 1-D stacking analysis, where only the area with positive signal was included. Consequently, the 3-D stacked line, includes faint extended signal missed by the moment-0 2σ regions used for the 1-D stacking analysis. Comparing the results of the 1-D stacked spectra with those of the 3-D stacked spectra it becomes clear that the broad component in the 1-D stacking is poorly constrained, due to the lack of the more extended signal that is included in the 3-D stacking.

5.2. A sub-sample with outflow signatures

In addition to simply stacking the full sample in search for an outflow signature, we have also developed a method for determining a sub-sample that maximises the possibility of detecting

Table 3: Results of our 1-D stacking analysis. The table includes the peak flux density (S_{peak}), FWHM, integrated flux density (S_{int}), and central frequency (ν_{cen}) of both the narrow and broad components of the stacked lines.

	Narrow comp.				Broad comp.			
	S_{peak} [mJy]	FWHM [km s ⁻¹]	S_{int} [Jy km s ⁻¹]	ν_{cen} [GHz]	S_{peak} [mJy]	FWHM [km s ⁻¹]	S_{int} [Jy km s ⁻¹]	ν_{cen} [GHz]
Full sample								
$w = 1$	7.1 ± 1.5	357 ± 40	2.7 ± 0.3	1 ± 7	0.7 ± 1.5	732 ± 596	0.5 ± 1.3	-13 ± 115
$w = 1/\sigma^2$	6.0 ± 0.8	368 ± 34	2.4 ± 0.4	0 ± 8	0.3 ± 0.8	885 ± 996	0.3 ± 0.8	3 ± 219
$w = 1/S_{\text{peak}}$	3.7 ± 2.3	356 ± 98	1.4 ± 0.9	0 ± 16	0.56 ± 2.39	671 ± 888	0.4 ± 1.8	-7 ± 149
max sub-sample								
$w = 1$	7.9 ± 0.6	352 ± 24	2.9 ± 0.3	2 ± 6	0.8 ± 0.6	999 ± 398	0.8 ± 0.7	-74 ± 124
$w = 1/\sigma^2$	6.9 ± 1.0	335 ± 33	2.5 ± 0.5	-4 ± 7	1.2 ± 1.1	745 ± 270	1.0 ± 1.0	42 ± 72
$w = 1/S_{\text{peak}}$	4.5 ± 0.9	311 ± 47	1.5 ± 0.4	1 ± 11	1.2 ± 0.9	787 ± 277	1.0 ± 0.8	-21 ± 67
min sub-sample								
$w = 1$	6.9 ± 0.2	375 ± 15	2.8 ± 0.1	0 ± 6
$w = 1/\sigma^2$	5.4 ± 0.2	386 ± 14	2.2 ± 0.1	0 ± 6
$w = 1/S_{\text{peak}}$	3.5 ± 0.2	390 ± 26	1.4 ± 0.1	0 ± 11

an outflow signature in the stacked spectrum. Under normal circumstances it is assumed that all stacked sources have the same properties, but in the case of outflows, the orientation of a bipolar outflow will impact on how it might be detected. If the outflow is oriented in or close to the plane of the sky, the radial component of the velocity will be relatively small and likely remain undetected. This means that even if all sample sources would have a high-velocity outflow, we would expect a fraction of these not to contribute to the stacked signal.

The sub-sample selection is done by randomly selecting subsets of n sources, where n is in the range 3–25, and repeated 10 000 times. For each of the 10 000 randomly selected sub-samples, we perform the same stacking analysis as described above. From the resulting stacked spectrum we select the “line-free” channels, defined to be at a distance of $2 \times \text{FWHM}$ of the center of the main line component. These are channels where we can expect to see only emission due to an outflow component. We then integrate over these channels at different radii from the center, within the range of $0.2\text{--}3''$ in steps of $0.2''$. The integrated flux density for each integration radius is saved as a grade for the sub-sample.

Once this is done for all 10 000 randomly selected sub-samples, each source in our sample is ranked based on the total sum of the grades of the sub-samples it was in at all integration radii. Sources with no outflow signal will be mostly in sub-samples with low grades, and will therefore have an overall low rank. We take the mean rank of all sources and define it as the lower limit for selection of the best sub-sample, i.e., the sub-sample of sources most likely to have signal from an outflow component (*max sub-sample*). We also define the sub-sample of least likely sources to have signal from an outflow component (*min sub-sample*), picked to have a rank below or equal to the mean.

The *max sub-sample* consists of 12 sources highlighted with boldface in Table 2. We note that the subsampling analysis was performed for both the 1-D and 3-D stacking analysis and returned the same sub-sample for both cases. These sources cover the same range in bolometric quasar luminosities, redshifts, IR luminosities and [C II] line properties as the full sample (see Fig. 5).

The stacked line of the *max sub-sample* is shown in the second column of Fig. 3 and the second row of Fig. 4. An outflow

component is found in both the 1-D and 3-D stacking results, for all three weighting schemes. In the case of the 1-D stacking analysis we find that the fit when including a broad component, is improved by 48%, 51%, 46% for weights of $w = 1$, $w = 1/\sigma_{\text{rms}}^2$, and $w = 1/S_{\text{peak}}$, respectively. We find that there is excess emission of $1.1\text{--}1.5\sigma$, depending on the weighting scheme used (see Tables 3 & 5). In the case of the 3-D stacking analysis the presence of a broad component is more pronounced. We find that including the broad component improves the fit by 62%, 57%, 48% for weights of $w = 1$, $w = 1/\sigma_{\text{rms}}^2$, and $w = 1/S_{\text{peak}}$, respectively. Furthermore, the significance of excess emission rises to $1.2\text{--}2.5\sigma$ (see Tables 4 & 5). The collapsed image (over $\pm 420\text{--}840 \text{ km s}^{-1}$) in Fig. 4, shows spatially extended emission, larger than what is seen for the narrow component (see contours), reaching $\sim 2''$ (see Fig. 4).

As discussed earlier, the 3-D stacking results are better at constraining the broad component signal compared to the 1-D stacking, due to the fact that it includes the more extended faint emission excluded in the 1-D stacking. Therefore, for the rest of this paper we only consider the 3-D stacking results.

We estimate the mean outflow rate (\dot{M}_{outf}) for the *max sub-sample*, based on the $w = 1$ 3-D stacking results. We use the equation of Hailey-Dunsheath et al. (2010) to calculate the outflow gas mass from the integrated [C II] luminosity of the broad component, which includes dependencies on the gas density (n), temperature (T), and abundance of C⁺ ions (X_{C^+}). Following Maiolino et al. (2012), and Cicone et al. (2015), we assume that $X_{\text{C}^+} = 1.4 \times 10^{-4}$, $T = 200 \text{ K}$, and $n \gg n_{\text{crit}}$ ($n_{\text{crit}} \sim 3 \times 10^3 \text{ cm}^{-3}$), which are typical of photo-dissociated regions. We calculate an estimate of the velocity (v_{outf}) of the outflow by taking $v_{\text{outf}} = 0.5 \times \text{FWHM}$, and take the radius of the extent of the outflow emission (R). By assuming that the velocity of the outflow is constant across the outflow, the dynamical time of the outflow can be defined as $\tau_{\text{dyn}} = R/v_{\text{outf}}$. Therefore, $\dot{M}_{\text{outf}} = M_{\text{outf}}/\tau_{\text{dyn}} = M_{\text{outf}} \times v_{\text{outf}}/R$. For the mean redshift of 6.236, a radius of $R = 11.5 \text{ kpc}$ ($2''$), and $v_{\text{outf}} = 493 \text{ km s}^{-1}$ calculate that $\dot{M}_{\text{outf}} = 45 \pm 21 M_{\odot} \text{ yr}^{-1}$. Since the properties of the broad component do not change significantly for the different weights, the calculated mass outflow rate will be similar for all weights.

To determine if a specific source in our *max sub-sample* is driving the outflow component emission and/or the shape of the

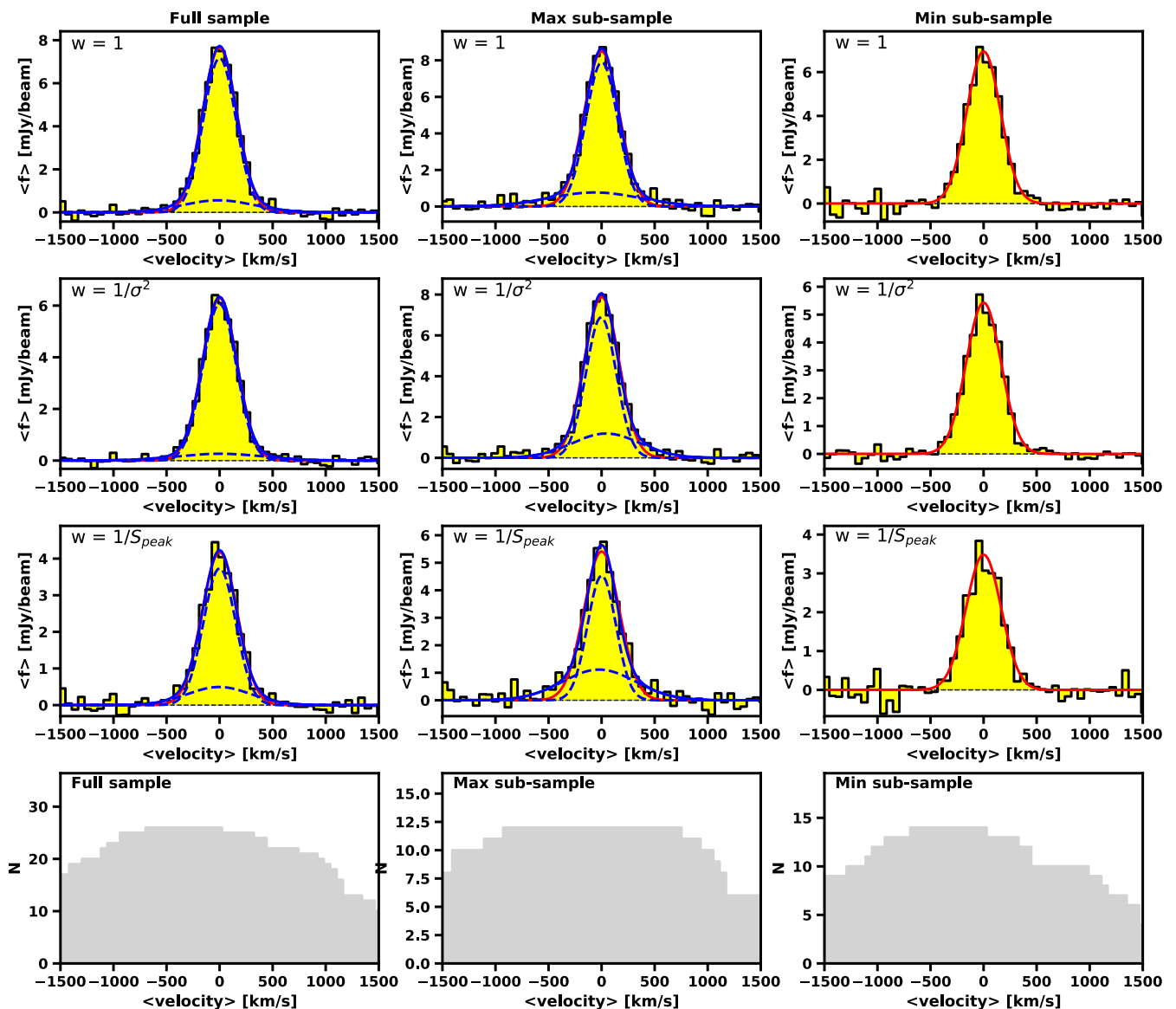


Fig. 3: Results from our 1-D stacking analysis. (*left*) The stacked spectra of the full sample, (*middle*) the *max sub-sample*, and (*right*) the *min-sub-sample*, using weights of $w = 1$ (1st row), $w = 1/\sigma_{\text{rms}}^2$ (2nd row), and $w = 1/S_{\text{peak}}$ (3rd row). On the last row we give the number of sources per channel of the stacked line.

extended emission, we perform a test. We repeat our stacking analysis as many times as the number of sources in the *max sub-sample*, and each time remove one of the sources. As a result we have the stacked lines and collapsed images for each source’s exclusion from the sub-sample. If one source is driving the observed results of the *max sub-sample*, then the stack without it will show significant differences to that of the *max sub-sample*. We find that none of the sources cause a significant difference in the extent of the high-velocity emission seen in the collapsed images, and none are specifically driving the shape and strength of the outflow component of the stacked [C II] line. Specifically, the FWHM, S_{peak} values of the broad component remain within 20% of those found for the stack of the complete *max sub-sample*, and remain within the error of the fitted values (see Table 4).

If we extract the line only from the central pixel then there is no evidence for an outflow, in agreement with the results by

Decarli et al. (2018). Taking the central pixel is equivalent to taking the flux within the beam for point like sources. This suggests that the emission of the outflow is spatially extended beyond the beam, as indicated by the collapsed image of the line wings in Fig. 4.

We have also looked into the stack of the sources excluded from the *max sub-sample* described above (right column of Fig. 3 and lower row of Fig. 4). A stack for these sources shows no evidence of an outflow component, and the line wing images show no significant traces of emission. This result also adds to the reasonableness of our *max sub-sample* selection, since it does not show any outflow signal, but also the average signal is not negative which could be the case if the signal in the *max sub-sample* was artificial.

In this analysis we have assumed that the outflow emission signature has the spectral profile of a single broad Gaussian,

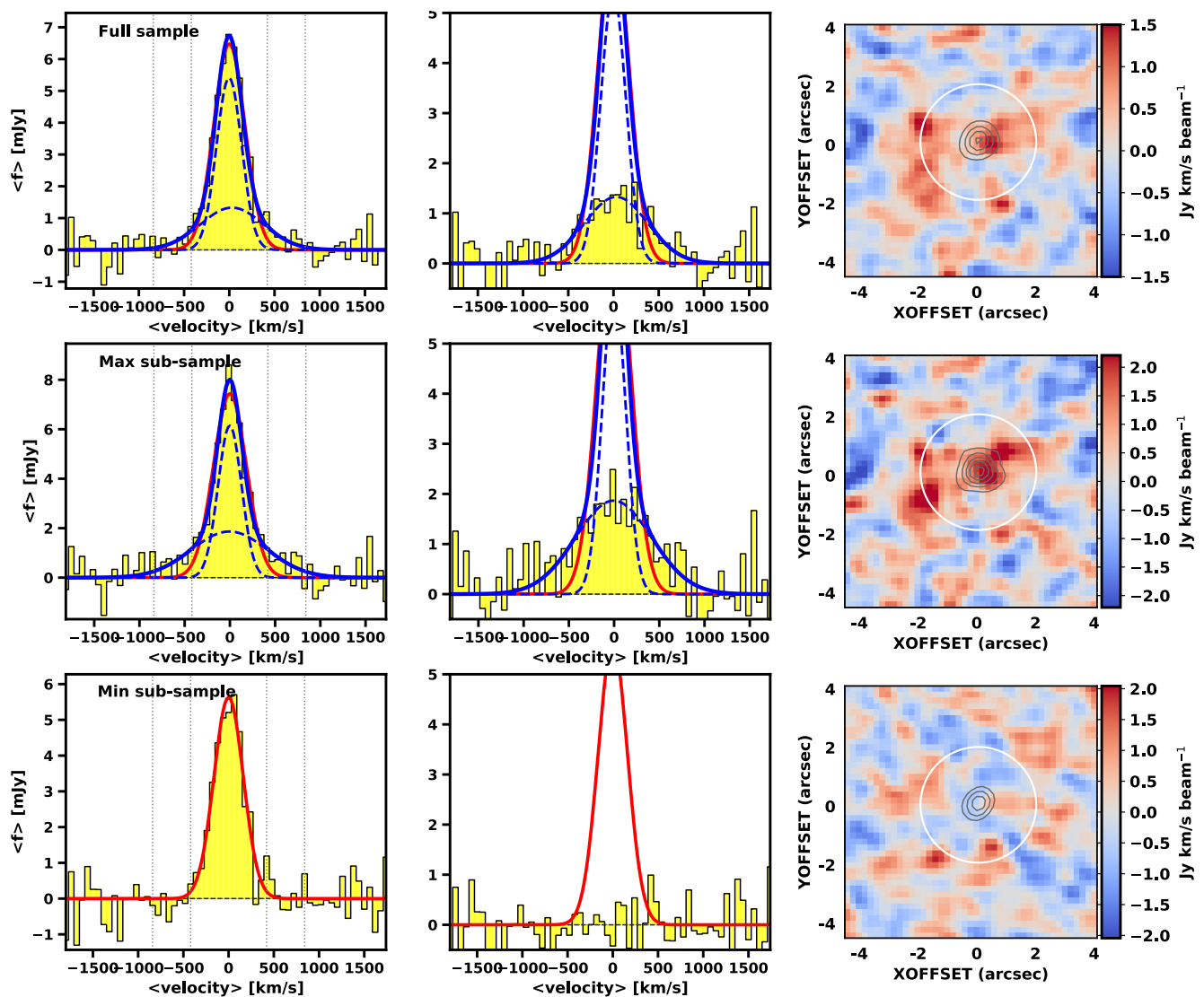


Fig. 4: Results from our 3-D stacking analysis, for $w = 1$. From left to right: the [C II] line extracted from the stacked cube within a $2''$ radius from the centre, a zoom-in view of the broad line component once the narrow component has been removed, combined image of the [C II] line wings from ± 420 – 840 km s $^{-1}$ (see vertical dotted lines in the spectrum), for the full sample (1st row), the *max sub-sample* (2nd row), and *min sub-sample* (3rd row). We also show the one (red curve) and two-component fits (blue solid and dashed curves) to the stacked line. The extent of the narrow component emission is shown with the black contours in the combined images, and the white circle corresponds to the area within a $2''$ radius from the centre.

which might not be the case for some or all of the quasars in our sample. Previous individual detections of outflows reported in the literature using e.g., CO, HCN, or [C II], show that the majority of the lines have nearly symmetric, broad emission lines, with a subset of results showing outflows dominated by emission only on the red or blue side of the main component (e.g., Cicone et al. 2014; Janssen et al. 2016). Apparent individual emission line components with a high velocity offset from the dominant line component could also be interpreted as an outflow signature (e.g., Fan et al. 2018). Furthermore, we have assumed that the broad component found is originating from the high-velocity gas of an outflow. However, it is possible that the high-velocity emission is not due to an outflow but for example, a gas flow between two interacting galaxies (for a detailed discussion see Gallerani et al. 2018). We know of one source included in our sample (PJ308-21) that has complex high-velocity structure

(e.g. Decarli et al. 2017). However, when this source is removed from our stacking analysis, the observed broad component and the spatial extent of the wings do not change significantly.

5.3. Testing the feasibility of detecting an outflow signal with our method.

To determine if the methods of our analysis are indeed capable of detecting an outflow component, we test their performance on mock samples with and without an outflow component. To test if our method can successfully retrieve the broad component signal, we perform our 1-D stacking analysis on a mock sample with [C II] lines that include a weak broad component. Based on the extracted spectra of our the observed sample, we use the one-component line fits of the observed lines, to which we add a broad line component of similar properties to what we find in our

Table 4: Results of our 3-D stacking analysis. Shown are the peak flux density (S_{peak}), FWHM, integrated flux density (S_{int}), and central frequency (ν_{cen}) of both the narrow and broad component of the stacked lines.

	Narrow component				Broad component			
	S_{peak} [mJy]	FWHM [km s $^{-1}$]	S_{int} [Jy km s $^{-1}$]	ν_{cen} [GHz]	S_{peak} [mJy]	FWHM [km s $^{-1}$]	S_{int} [Jy km s $^{-1}$]	ν_{cen} [GHz]
Full sample								
$w = 1$	5.41 ± 0.89	328 ± 41	1.9 ± 0.4	-2 ± 10	1.33 ± 0.92	820 ± 261	1.1 ± 0.9	30 ± 65
$w = 1/\sigma_{\text{rms}}^2$	6.54 ± 0.43	373 ± 23	2.6 ± 0.2	2 ± 6	0.37 ± 0.44	1029 ± 614	0.5 ± 0.6	-100 ± 213
$w = 1/S_{\text{peak}}$	2.93 ± 1.05	300 ± 82	0.9 ± 0.4	-19 ± 22	1.62 ± 1.08	724 ± 211	1.2 ± 0.9	56 ± 75
max sub-sample								
$w = 1$	6.14 ± 0.69	305 ± 36	2.0 ± 0.3	-1 ± 10	1.87 ± 0.68	986 ± 210	2.0 ± 0.8	-5 ± 58
$w = 1/\sigma_{\text{rms}}^2$	7.53 ± 0.4	348 ± 22	2.8 ± 0.2	2 ± 7	0.81 ± 0.33	1427 ± 408	1.2 ± 0.6	-100 ± 138
$w = 1/S_{\text{peak}}$	3.05 ± 0.85	182 ± 62	0.6 ± 0.3	-24 ± 20	3.31 ± 0.69	775 ± 116	2.7 ± 0.7	10 ± 38
min sub-sample								
$w = 1$	5.63 ± 0.31	383 ± 24	2.3 ± 0.2	0 ± 10
$w = 1/\sigma_{\text{rms}}^2$	6.43 ± 0.21	390 ± 14	2.7 ± 0.1	0 ± 6
$w = 1/S_{\text{peak}}$	3.61 ± 0.39	378 ± 47	1.4 ± 0.2	0 ± 20

 Table 5: The significance of the excess emission over the one component fit to the spectra (red curve in Fig. 3 & 4), for the Full sample and *max sub-sample* in all three weighting schemes used.

	1-D stacking	3-D stacking
Full sample		
$w = 1$	0.7σ	1.5σ
$w = 1/\sigma_{\text{rms}}^2$	0.6σ	1.3σ
$w = 1/S_{\text{peak}}$	0.4σ	1.1σ
max sub-sample		
$w = 1$	1.3σ	2.1σ
$w = 1/\sigma_{\text{rms}}^2$	1.5σ	2.5σ
$w = 1/S_{\text{peak}}$	1.2σ	1.2σ

stacking results, with 2 times the width and 0.1 times the peak flux density of the main line component. For 10 000 iterations, we add random noise to the individual [C II] lines, based on the range of the observed rms, and stack following our 1-D stacking analysis. We then determine if we can detect excess emission due to a broad component in the stacked spectra, following the method described in section 5.1. We find excess emission due to a broad component with only a weak significance of $< 3\sigma$, with 75% of iterations having an excess emission of $1 - 2\sigma$ for stacks with weights of $w = 1$ and $w = 1/\sigma_{\text{rms}}^2$. However, a weight of $w = 1/S_{\text{peak}}$ seems to suppress the signal, with the detectability of excess emission dropping to 20% for a $1 - 2\sigma$ significance (see figures in Appendix A). It is worth noting however, that if assuming a stronger initial broad component, with 3 times the width and 0.2 times the peak flux density of the main line component, then our method retrieves a strong broad component in the stacks. In this case an excess emission of $> 5\sigma$ for $> 99\%$ of iterations, for stacks with weights of $w = 1$ and $w = 1/\sigma_{\text{rms}}^2$, and $> 3\sigma$ for 35% of iterations for $w = 1/S_{\text{peak}}$.

To test if it is possible that the outflow component found in our results could be created by stacked noise and is not a real signal, we perform a similar simulation. Based on the one-component fit to the [C II] lines of our sample, we create a mock sample with the same line properties, and without an added outflow component. We then add random noise to each based on the

range of the observed rms. We perform our 1-D stacking analysis on this mock sample 10 000 times, each time re-applying randomly selected noise levels. Then we attempt a two-component fit to each stacked line and determine if a broad line component is found and if it has comparable properties to the one found in our analysis of the observed data. This is done for all three weighting schemes. We find that, depending on the weight scheme used, 14-17% of the iterations return a $> 0.4\sigma$ excess signal in the stacked lines (see Appendix A).

6. Discussion

6.1. Spectral line stacking methods

At the high redshifts covered in our study the spatial information available is limited. Therefore, our analysis will primarily be sensitive to the information that can be derived from the velocity characteristics of the observed lines. Hence our type of analysis is relevant for outflows that have velocities higher than that of the host galaxy emission, and low-velocity outflows will not be detected.

As the aim of the stacking is to search for a faint broad emission line component, it is imperative to understand the effect of stacking data where the main (bright) component has varying line widths. If spectral lines, such as those of the data used here, are simply stacked, it could result in the detection of an artificial broad component. To test the effect of the varying FWHM values of the lines stacked on the final result, we create a mock sample with the observed line properties of the observed sample, without adding an outflow component. We perform our stacking analysis on this mock sample 10 000 times, each time re-applying randomly selected noise levels within the range of observed rms. For each iteration we perform both straightforward stacking, and stacking using our rebinning method. For the resulting stacked spectra we attempt two-component fitting to determine if a significant broad component is found. We find that for the simple/straightforward stacking analysis, excess emission due to a broad component is found at $> 2\sigma$ 2-5% of the time. However, we find that these cases are due to the noise of the stacked spectrum. If we repeat the exercise without including noise in the spectra, then a broad component is not found. It is worth noting that even if a significant broad component is not fitted in the majority of the cases, there is

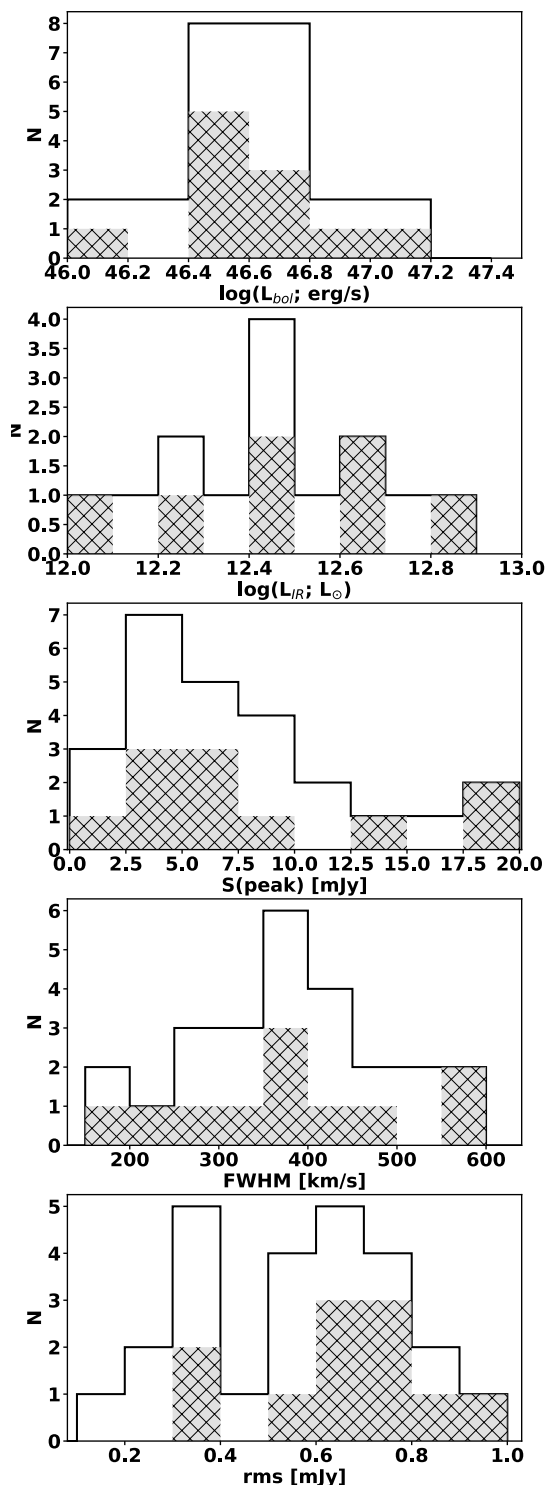


Fig. 5: Here we show the distribution of the properties of the sources in the *max sub-sample* (filled in regions) in comparison to the full sample of this study (main histogram). From top to bottom we compare: the bolometric luminosity of the quasars (L_{bol}), the IR (8–1000 μm) luminosity of the galaxies (L_{IR}), the S_{peak} , the FWHM, and the rms of the of the individual [C II] lines (before the velocity rebinning). It is evident that the *max sub-sample* covers a wide range of values in all properties, and is not skewed towards the brightest quasars, specific line-widths or line strength. The *max sub-sample* does seem to prefer higher rms values, but this is restricted by small number statistics.

still low significance ($< 1\sigma$) excess emission in the line wings that the single component gaussian cannot fit (see examples in Appendix A).

Recently, there have been two other studies looking at similar samples of high- z quasars with [C II] (Decarli et al. 2018; Bischetti et al. 2019). In Decarli et al. (2018) a sample of $z \sim 6$ quasars observed with [C II] is presented, and a brief analysis on the presence of outflows is included. The overall analysis is not that different to our own, as they also use velocity rebinning before stacking, but have only stacked the spectra extracted from the central pixel of each source. They report no evidence for a broad component in the stacked spectra, which is consistent with the results of our 1-D stacking analysis of the Full sample. However, as we have demonstrated in this paper, it is imperative to take into account the emission from the entire extent of the galaxy, as the outflow emission may be originating from an extended region.

Bischetti et al. (2019) used archival data of quasars in the wider redshift range of $4.5 < z < 7.1$, to search for outflow signatures in the stacked spectra. However, it is not clear how the archive data have been treated; as noted previously, we needed to manually re-calibrate 70% of the archive observations of our sample. The individual spectra were integrated over a region equivalent of four times the beam size, and were stacked without velocity rebinning but with a weighting scheme of $1/\sigma_{\text{rms}}^2$ for each channel of each spectrum. Evidence for a broad outflow component are found, in agreement with our conclusions, but with a stronger significance. The higher significance of the broad component found in the Bischetti et al. (2019) analysis could be due to the absence of velocity rebinning to account for the range in the FWHM values of the lines stacked, which could result to an overestimate of the flux and FWHM of the broad component. However, it could also be due to the larger sample used in their analysis.

Even though velocity re-binning is important in order to not introduce artificial signal to the broad line emission, it also implies that the line width of the broad line component is roughly proportional to that of the main component. Consequently, our analysis can detect a broad component, but it will not be based on the absolute value of the line width, but rather on the mean of the velocity axis of the spectra stacked. However, current available spectroscopic data lack the sensitivity to fully detect individual outflows, and spectral stacking is the only available method at present to determine the presence of outflow signatures.

6.2. Should we expect to see outflows in all high- z quasars?

As discussed previously, we find only a tentative signal for an outflow component when stacking the full sample of $z \sim 6$ quasars, but find that for a specific subsample of sources we can detect a significant outflow component. This would suggest that either not all $z \sim 6$ quasars have outflows (at least at the time of observation), or there are effects that inhibit the observability of present outflows.

Recently, a study by Barai et al. (2018) using zoom-in hydrodynamical simulations to determine the effect of outflows on the host galaxy and surrounding environment of quasars at $z \geq 6$, has demonstrated that outflows could indeed be a dominant feature of high redshift quasars. Even though the quasar host galaxies at $z \sim 6$ are accreting significant amounts of cosmic gas, AGN feedback succeeds in reducing the inflow by $\sim 12\%$, with $\sim 20\%$ of the quasar outflows having speeds greater than the escape velocity of 500 km s^{-1} , subsequently

succeeding in ejecting gas out of the host galaxy, and regulating the on-going star formation (Barai et al. 2018).

6.2.1. Outflow orientation

The presence, strength, and width of a broad line component due to outflow emission will be dependent on the orientation of the outflow with respect to the observer’s line of sight. Indeed, in a recent study by Roberts-Borsani & Saintonge (2018) investigating cold gas inflows and outflows around galaxies in the local Universe, it was found that outflows were detected only for outflow angles $< 50^\circ$ in respect to the line of sight, while for $> 60^\circ$ it was **only** possible to detect inflows.

To test how orientation angles could affect the observability of an outflow component in the stacked spectra we run a simple Monte-Carlo test. In its most simplistic form, we assume that all galaxies in the sample have the same values of peak flux density and FWHM of their lines and have the same outflow component.

We first define a line profile that is a combination of a narrow and broad component. For the narrow component we assume $S_{\text{peak}} = 10 \text{ mJy}$ and $\text{FWHM} = 400 \text{ km s}^{-1}$. For the broad component, we assume five different FWHM values (800, 900, 1000, 1100, 1200 km s^{-1}) and repeat the test for each.

For each of the broad component FWHM values, we run 1000 iterations, in each of which we select 30 random angles between $10\text{--}80^\circ$ (simplistic assumption to avoid a blazar, 0° , and obscured quasar, 90° , types). We combine the selected random orientation angles with the defined line profile to create a mock sample of 30 galaxies, and add random noise with rms of $\sim 0.5 \text{ mJy}$, similar to what is seen in the observed sample. We then stack the spectra following the same methods as described in sect. 4. We fit the resulting stacked spectral line with a single and double-component Gaussian function, and calculate the respective χ^2 values of the fits, and the significance of the broad component emission.

We find that an excess emission due to a broad component, of $> 2\sigma$ significance is retrieved for 27 – 50% of the iterations, for the cases where we have assumed an initial broad component with $\text{FWHM} > 1000 \text{ km s}^{-1}$. For an initial broad component with FWHM of 800 and 900 km s^{-1} , a broad component in the stack with $> 1\sigma$ is found in $> 60\%$ of iterations (see Figures A.4 & A.6 in Appendix A).

6.2.2. Choice of outflow tracers

The choice of a tracer is an important part in all studies aiming to determine the presence and properties of outflows in galaxies. The recent studies on the presence of outflows in the most distant quasars (this work; Decarli et al. 2018; Bischetti et al. 2019) all show different results, and none can reproduce the very strong signal seen in SDSS J1148+5251 (e.g. Cicone et al. 2015). Therefore, it is important to consider if [C II] is indeed a suitable tracer of outflows. Are the weak outflow signatures that we observe due to the choice of [C II] as a tracer? Is there a better tracer for outflows?

[C II] $158\mu\text{m}$ is a tracer of atomic gas at typical densities of $2.8 \times 10^3 \text{ cm}^{-3}$ with temperatures of $\sim 92 \text{ K}$. It conveniently falls within the ALMA bands at $z \sim 6$, and therefore is easy to observe and proves a very useful tracer, especially for quasar studies (see review by Carilli & Walter 2013). However, at lower redshifts, there is a variety of more commonly used gas tracers used to de-

tect outflow signatures of AGN, such as ^{12}CO tracing molecular gas.

[C II] emission can originate from ionised, atomic, and molecular regions; however, both low and high redshift observational and theoretical work argue that the majority of [C II] emission (70–90%) originates from neutral atomic gas (e.g., Croxall et al. 2017; Olsen et al. 2015; Lagache et al. 2018). Although, there has been observational evidence of [C II] emission from ionised regions (e.g., Contursi et al. 2013; Decarli et al. 2014). [C II] emission has also been found to trace molecular gas that is “CO-faint” due to the disassociation of the CO molecules from far-ultraviolet emission (e.g., Jameson et al. 2018). However, Lagache et al. (2018) highlight that the [C II] emission at redshifts $z > 6$ can be strongly affected by attenuation from the cosmic microwave background; although it is mostly warm and low density gas that is affected by this. [C II] $158\mu\text{m}$ has been successful in detecting outflows in a few nearby galaxies (e.g., Contursi et al. 2013; Kreckel et al. 2014), but at redshifts of $z \sim 6$ the only example of a quasar outflow detected with [C II] is J1148+5251 (e.g., Maiolino et al. 2012; Cicone et al. 2015).

It is possible that CO cannot survive in the outflow regions; however, CO(5-4) has been seen in an ionised outflow region (e.g., Brusa et al. 2018, similar result found in Fogasy et al., in prep) at high redshifts, and there are plenty of nearby galaxies with resolved molecular outflows traced with multiple CO transitions (e.g., Alatalo et al. 2011; Aalto et al. 2012; Cicone et al. 2012, 2014; Feruglio et al. 2015; Veilleux et al. 2013, 2017).

Although H α and [O III], as well as X-ray emission can directly trace the shocked and ionised regions caused by the outflows, and hence may be a more direct probe, such observations are currently impossible at such high redshifts. There is currently only one tentative detection of hot gas in the X-ray (SDSS J1030+0524, Nanni et al. 2018). However, future JWST projects may be able to probe the ionised gas in high redshift outflows.

Overall, due to the lack of systematic studies on the topic it remains unclear if [C II] - so far the most commonly studied outflow tracer at high- z - is a good tracer of outflows in distant galaxies. However, with the sensitivity of ALMA it is possible to have systematic studies in the future, to address this.

6.3. The presence of outflows in high-redshift quasars.

Individual studies of high-redshift quasars have revealed some evidence for outflows based on [C II] and/or CO observations. At a redshift of $z \sim 6.4$, the luminous quasar SDSS J1148+5251 shows a strong [C II] broad component indicating the presence of an outflow with velocities of up to 1400 km s^{-1} and extending to distances of $\sim 30 \text{ kpc}$ (Maiolino et al. 2012; Cicone et al. 2015). At the lower redshifts of $z \sim 1.4$, $z \sim 1.6$, and $z \sim 3.9$, Vayner et al. (2017), Brusa et al. (2018), and Feruglio et al. (2017) report the detection of a molecular outflow traced with CO. In the first two cases the outflow velocities are $600\text{--}700 \text{ km s}^{-1}$, while in the third case the outflow velocity reaches up to $\sim 1300 \text{ km s}^{-1}$. At redshifts of $z \sim 1\text{--}3$ there are also numerous detections of ionised outflows traced with [O III] (e.g., Harrison et al. 2012, 2016; Brusa et al. 2016; Carniani et al. 2016; Vayner et al. 2017).

In studies of lower redshift AGN outflows of $z < 0.2$ using [O III] ionised gas tracer, there is a prevalence of outflows in both luminous AGN (e.g., Harrison et al. 2014) and among ULIRGs hosting AGN (e.g., Rose et al. 2018; Tadhunter et al. 2018; Spence et al. 2018), with typical line widths of $\approx 600\text{--}1500 \text{ km s}^{-1}$ and $\approx 500\text{--}2500 \text{ km s}^{-1}$. Similarly, molecular outflow studies of nearby quasar galaxies using CO, HCN, and other

molecular tracers, have found outflows with velocities reaching $\approx 750 - 1100 \text{ km s}^{-1}$ (e.g., Cicone et al. 2014; Aalto et al. 2015; Veilleux et al. 2017).

For the max sub-sample we find a mean outflow velocity of $\sim 337-713 \text{ km s}^{-1}$, consistent with observations of both ionised and molecular outflows in single objects up to $z \sim 2.5$. Our results are also consistent with the range of mean outflow velocities reported in Bischetti et al. (2019). We find that the ratio of the peak flux densities of the outflow over the main component found for our full sample and max-sub-sample at $2''$ both range between $\approx 0.1-0.5$, and is highly dependent on the weighting scheme using. This is in agreement with the relative ratio of 0.14 seen in J1148+5251 at $z \sim 6$ (e.g., Maiolino et al. 2005; Cicone et al. 2015), while larger than seen in Mrk231 (≈ 0.067) when using the different tracer CO(1-0) in the nearby Mrk231 (e.g., Cicone et al. 2012).

In order to improve our understanding on the prevalence of outflows at $z \sim 6$ and above we will need deeper observations of quasar samples in both [C II] and CO, as well as tracers of the warm ionised medium. However, a multi-tracer approach is costly in terms of observing time, and thus the methods presented in this work provide a useful step towards designing the relevant observations. Large emission line surveys of high-redshift quasars can be combined with the sub-sampling method presented in Sect. 5.2, to determine the more likely candidates to have outflows for deeper multi-phase observations. Apart from the ability to select a sub-sample of most likely sources to have an outflow, sub-sampling can also help to take into account potential effects such as orientation or selection effects.

7. Conclusions

We have carried out a study of spectral stacking [C II] ALMA archive observations of $z \sim 6$ optically selected quasars, to search for faint outflow signal. We performed this analysis for both extracted spectra and full spectral cubes, allowing for the extraction of stacked spectra over different regions. We also performed a sub-sampling technique to identify the sub-sample of our sources that maximise the broad component signal when stacked.

Specifically:

- We find tentative broad component signal for our full sample of 26 quasars. The stacked spectrum has a broad component of $\text{FWHM} > 700 \text{ km s}^{-1}$ with a total line flux density of $S_{\text{int}} > 0.5 \text{ Jy km s}^{-1}$. The excess emission, above a single component fit to the stacked line, corresponds to $0.4-1.5\sigma$, depending on the weighting scheme used in the stack.
- We identify a sub-sample of 12 sources, which maximise the broad component signal when stacked. The broad component detected in this sub-sample is characterised by an average $\text{FWHM} > 775 \text{ km s}^{-1}$, and $S_{\text{int}} > 1.2 \text{ Jy km s}^{-1}$. The excess emission is detected at $1.2-2.5\sigma$, depending on the weighting scheme used. These results are consistent with results of individual sources at low and high redshifts.
- We test if our methods could introduce artificial outflow signal when stacking, by creating mock sampled based on the observed [C II] line properties of our sample. In this mock sample there is no broad component included. We find that the probability to falsely detect a broad component with an excess emission of $> 0.4\sigma$ is $< 17\%$.

Using spectral line stacking as a tool for this type of studies has the following implications:

- Spectral line stacking is a meaningful tool for searching for outflows in the spectra of quasars. Given that the redshift is well known because of the bright line emission from the host galaxies, there will be no significant velocity offsets that would dilute the emission from the fainter (broad) component. However, it is important to take into account the varying line width of the main line component in order to avoid introducing additional broad spectral features.
- As outflows are thought to be anisotropic emission that is typically seen as bi-polar, and for which the orientation is most likely random, it is expected that at least a sub-set of the sample will not contribute significant or any emission from the outflow to the stacked spectrum. For instance, if the outflow is aligned close to or on the line of sight, the projected radial velocity might be the same or less than that of the main component. For a sample typically of the size studied here, if the orientation is random, it would be possible to obtain an outflow signal if the outflow velocity is larger than twice the main component line width. To take into account the fact that not all sources will be contributing significantly, we developed a tool for identifying the sub-sample most likely to have outflow signatures in its stacked spectrum.
- We have used the assumption that the outflow is characterised by a high velocity component with a line width significantly larger than that of main line, and such spectral signatures are seen in some local AGNs that have detected outflows. However, it is possible that outflows may have other spectral characteristics, that will not be traced with our methods.

This type of study represents a step towards better insights in outflows and possible feedback in massive galaxies, however, to gain full insights the next steps will need to include direct detection of individual sources as well as the detection of multiple outflow tracers.

Acknowledgements. We thank the anonymous referee for their instructive comments for the improvement of this paper. FS acknowledges support from the Nordic ALMA Regional Centre (ARC) node based at Onsala Space Observatory. The Nordic ARC node is funded through Swedish Research Council grant No 2017-00648. KK acknowledges support from the Swedish Research Council and the Knut and Alice Wallenberg Foundation. This paper makes use of the following ALMA data: ADS/JAO.ALMA#2015.0.00606.S, ADS/JAO.ALMA#2015.0.00997.S and ADS/JAO.ALMA#2015.0.01115.S. ALMA is a partnership of ESO (representing its member states), NSF (USA) and NINS (Japan), together with NRC (Canada), MOST and ASIAA (Taiwan), and KASI (Republic of Korea), in cooperation with the Republic of Chile. The Joint ALMA Observatory is operated by ESO, AUI/NRAO and NAOJ. This research made use of APLpy, an open-source plotting package for Python (Robitaille & Bressert 2012).

References

- Aalto, S., Garcia-Burillo, S., Muller, S., et al. 2012, A&A, 537, A44
Aalto, S., Martín, S., Costagliola, F., et al. 2015, A&A, 584, A42
Alatalo, K., Blitz, L., Young, L. M., et al. 2011, ApJ, 735, 88
Bañados, E., Venemans, B. P., Decarli, R., et al. 2016, ApJS, 227, 11
Bañados, E., Venemans, B. P., Morganson, E., et al. 2014, AJ, 148, 14
Barai, P., Gallerani, S., Pallottini, A., et al. 2018, MNRAS, 473, 4003
Barcos-Muñoz, L., Aalto, S., Thompson, T. A., et al. 2018, ApJ, 853, L28
Bischetti, M., Maiolino, R., Fiore, S. C. F., Piconcelli, E., & Fluetsch, A. 2019, ArXiv e-prints, arXiv:1806.00786v4
Brusa, M., Cresci, G., Daddi, E., et al. 2018, A&A, 612, A29
Brusa, M., Perna, M., Cresci, G., et al. 2016, A&A, 588, A58
Carilli, C. L. & Walter, F. 2013, ARA&A, 51, 105
Carnall, A. C., Shanks, T., Chehade, B., et al. 2015, MNRAS, 451, L16
Carniani, S., Marconi, A., Maiolino, R., et al. 2016, A&A, 591, A28
Cicone, C., Feruglio, C., Maiolino, R., et al. 2012, A&A, 543, A99
Cicone, C., Maiolino, R., Gallerani, S., et al. 2015, A&A, 574, A14
Cicone, C., Maiolino, R., Sturm, E., et al. 2014, A&A, 562, A21

- Contursi, A., Poglitsch, A., Gracia Carpio, J., et al. 2013, *A&A*, 549, A118
- Croxall, K. V., Smith, J. D., Pellegrini, E., et al. 2017, *ApJ*, 845, 96
- De Rosa, G., Decarli, R., Walter, F., et al. 2011, *ApJ*, 739, 56
- Decarli, R., Walter, F., Carilli, C., et al. 2014, *ApJ*, 782, L17
- Decarli, R., Walter, F., Venemans, B. P., et al. 2017, *Nature*, 545, 457
- Decarli, R., Walter, F., Venemans, B. P., et al. 2018, *ApJ*, 854, 97
- Fabian, A. C. 2012, *ARA&A*, 50, 455
- Fan, L., Knudsen, K. K., Fogasy, J., & Drouart, G. 2018, *ApJ*, 856, L5
- Fan, X., Narayanan, V. K., Lupton, R. H., et al. 2001, *AJ*, 122, 2833
- Fan, X., Strauss, M. A., Richards, G. T., et al. 2006, *AJ*, 131, 1203
- Feruglio, C., Ferrara, A., Bischetti, M., et al. 2017, *A&A*, 608, A30
- Feruglio, C., Fiore, F., Carniani, S., et al. 2015, *A&A*, 583, A99
- Gallerani, S., Pallottini, A., Feruglio, C., et al. 2018, *MNRAS*, 473, 1909
- Hailey-Dunsheath, S., Nikola, T., Stacey, G. J., et al. 2010, *ApJ*, 714, L162
- Harrison, C. M., Alexander, D. M., Mullaney, J. R., et al. 2016, *MNRAS*, 456, 1195
- Harrison, C. M., Alexander, D. M., Mullaney, J. R., & Swinbank, A. M. 2014, *MNRAS*, 441, 3306
- Harrison, C. M., Alexander, D. M., Swinbank, A. M., et al. 2012, *MNRAS*, 426, 1073
- Jameson, K. E., Bolatto, A. D., Wolfire, M., et al. 2018, *ApJ*, 853, 111
- Janssen, A. W., Christopher, N., Sturm, E., et al. 2016, *ApJ*, 822, 43
- Jiang, L., McGreer, I. D., Fan, X., et al. 2015, *AJ*, 149, 188
- Jiang, L., McGreer, I. D., Fan, X., et al. 2016, *ApJ*, 833, 222
- King, A. & Pounds, K. 2015, *ARA&A*, 53, 115
- Knudsen, K. K., Richard, J., Kneib, J.-P., et al. 2016, *MNRAS*, 462, L6
- Kreckel, K., Armus, L., Groves, B., et al. 2014, *ApJ*, 790, 26
- Kurk, J. D., Walter, F., Fan, X., et al. 2007, *ApJ*, 669, 32
- Lagache, G., Cousin, M., & Chatzikos, M. 2018, *A&A*, 609, A130
- Maiolino, R., Cox, P., Caselli, P., et al. 2005, *A&A*, 440, L51
- Maiolino, R., Gallerani, S., Neri, R., et al. 2012, *MNRAS*, 425, L66
- Matsuoka, Y., Onoue, M., Kashikawa, N., et al. 2016, *ApJ*, 828, 26
- Mazzucchelli, C., Bañados, E., Venemans, B. P., et al. 2017, *ApJ*, 849, 91
- McMullin, J. P., Waters, B., Schiebel, D., Young, W., & Golap, K. 2007, in *Astronomical Society of the Pacific Conference Series*, Vol. 376, *Astronomical Data Analysis Software and Systems XVI*, ed. R. A. Shaw, F. Hill, & D. J. Bell, 127
- Mortlock, D. J., Patel, M., Warren, S. J., et al. 2009, *A&A*, 505, 97
- Mullaney, J. R., Alexander, D. M., Goulding, A. D., & Hickox, R. C. 2011, *MNRAS*, 414, 1082
- Nanni, R., Gilli, R., Vignali, C., et al. 2018, *A&A*, 614, A121
- Olsen, K. P., Greve, T. R., Narayanan, D., et al. 2015, *ApJ*, 814, 76
- Omont, A., Willott, C. J., Beelen, A., et al. 2013, *A&A*, 552, A43
- Reed, S. L., McMahon, R. G., Banerji, M., et al. 2015, *MNRAS*, 454, 3952
- Roberts-Borsani, G. W. & Saintonge, A. 2018, *ArXiv e-prints* [arXiv:1807.07575]
- Robitaille, T. & Bressert, E. 2012, *APLpy: Astronomical Plotting Library in Python*, *Astrophysics Source Code Library*
- Rose, M., Tadhunter, C., Ramos Almeida, C., et al. 2018, *MNRAS*, 474, 128
- Runnoe, J. C., Brotherton, M. S., & Shang, Z. 2012, *MNRAS*, 426, 2677
- Rupke, D. S. N. & Veilleux, S. 2011, *ApJ*, 729, L27
- Schaye, J., Crain, R. A., Bower, R. G., et al. 2015, *MNRAS*, 446, 521
- Sijacki, D., Vogelsberger, M., Genel, S., et al. 2015, *MNRAS*, 452, 575
- Somerville, R. S., Hopkins, P. F., Cox, T. J., Robertson, B. E., & Hernquist, L. 2008, *MNRAS*, 391, 481
- Spence, R. A. W., Tadhunter, C. N., Rose, M., & Rodríguez Zaurín, J. 2018, *MNRAS*, 478, 2438
- Stanley, F., Harrison, C. M., Alexander, D. M., et al. 2018, *MNRAS*, 478, 3721
- Sturm, E., González-Alfonso, E., Veilleux, S., et al. 2011, *ApJ*, 733, L16
- Tadhunter, C., Rodríguez Zaurín, J., Rose, M., et al. 2018, *MNRAS*, 478, 1558
- Vayner, A., Wright, S. A., Murray, N., et al. 2017, *ApJ*, 851, 126
- Veilleux, S., Bolatto, A., Tombesi, F., et al. 2017, *ApJ*, 843, 18
- Veilleux, S., Meléndez, M., Sturm, E., et al. 2013, *ApJ*, 776, 27
- Venemans, B. P. 2017, *The Messenger*, 169, 48
- Venemans, B. P., Bañados, E., Decarli, R., et al. 2015, *ApJ*, 801, L11
- Venemans, B. P., Decarli, R., Walter, F., et al. 2018, *The Astrophysical Journal*, 866, 159
- Venemans, B. P., McMahon, R. G., Walter, F., et al. 2012, *ApJ*, 751, L25
- Venemans, B. P., Walter, F., Decarli, R., et al. 2017, *ApJ*, 845, 154
- Venemans, B. P., Walter, F., Zschaechner, L., et al. 2016, *ApJ*, 816, 37
- Wang, R., Wagg, J., Carilli, C. L., et al. 2013, *ApJ*, 773, 44
- Wang, R., Wagg, J., Carilli, C. L., et al. 2011, *ApJ*, 739, L34
- Wang, R., Wu, X.-B., Neri, R., et al. 2016, *ApJ*, 830, 53
- Willott, C. J., Bergeron, J., & Omont, A. 2017, *ApJ*, 850, 108
- Willott, C. J., Delorme, P., Omont, A., et al. 2007, *AJ*, 134, 2435
- Willott, C. J., Delorme, P., Reylé, C., et al. 2010, *AJ*, 139, 906
- Willott, C. J., Omont, A., & Bergeron, J. 2013, *ApJ*, 770, 13

Appendix A: Tests on the spectral stacking methods and orientation effects

In section 5.3 we discussed two tests on the spectral stacking analysis using mock samples. One where all the lines in our mock sample included a broad component below the noise, and one where no broad component was included in the mock sample. Here we show the fraction of iterations showing excess emission due to a broad component at different significance levels (Figure A.1), and example stacked spectra from these tests (Figure A.3). As discussed in section 5.3, our spectral stacking analysis successfully retrieves a broad component in the stacked lines of the mock samples with an outflow component 75% of the time with an excess emission of $1 - 2\sigma$ for weights of $w = 1$ and $w = 1/\sigma_{rms}^2$. But for $w = 1/S_{peak}$, its only able to retrieve excess emission at $1 - 2\sigma$ 20% of the time. In the case of the mock samples without an outflow component included, there is no excess emission detected at $> 2\sigma$, and only $< 17\%$ of the time do we retrieve excess emission between $> 0.4\sigma$.

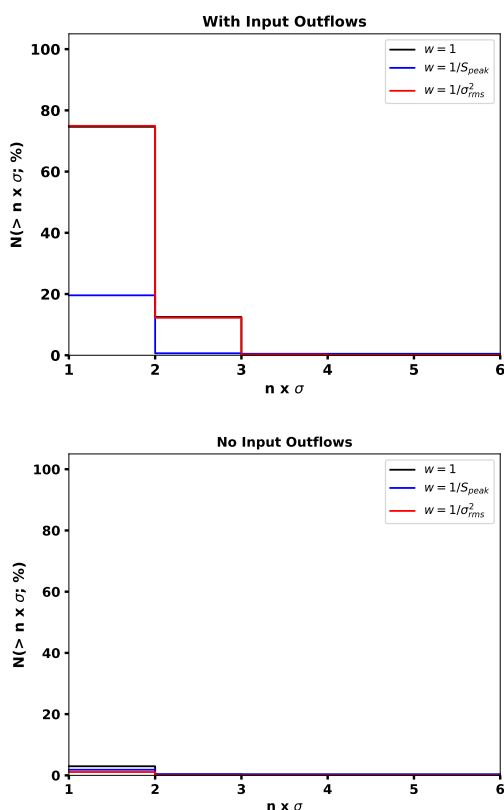


Fig. A.1: Histogram of the fraction of iterations that the stacked spectra shows excess emission at significance levels greater than $n \times \sigma$. (*top*) The results of our test on stacking mock samples where all sources had a broad component below the noise levels. (*bottom*) The results of our test on stacking mock samples where all sources had no added broad component. We show the results for stacking with all three of the weights assumed in this work.

In section 6.1 we discussed the effect of stacking lines without taking into account the range of line widths of the sample, i.e. without applying velocity rebinning on the lines before stacking. In this case we did a test on stacking a mock sample of lines with similar properties to our sample and with no broad component, without applying velocity rebinning. We repeated the exercise

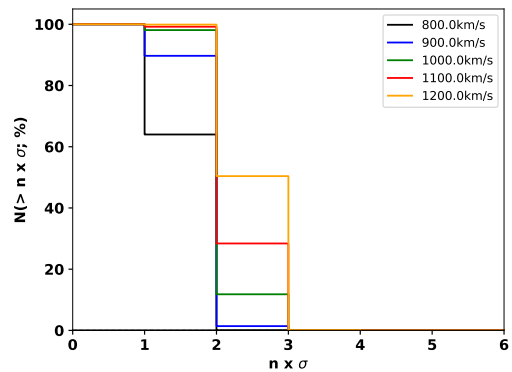


Fig. A.2: Histogram of the fraction of iterations that the stacked spectra shows excess emission at significance levels greater than $n \times \sigma$. In this case we show the results of our outflow orientation test. Each colour corresponds to a different initial FWHM of the broad component.

with and without the inclusion of noise in the mock samples. If there is no noise included, the stacked line does not have a broad component in any of the iterations. When including the noise, we retrieve $> 2\sigma$ excess emission only 2–5% of the time. We show examples of the stacked spectra from this test in Fig. A.3 (last row).

In section 6.2.1 we discussed the effect that the orientation of the outflows could have on the detections of a broad component signature in the stacked lines (see section 6.2.1). In Fig. A.2 we show the fraction of iterations with excess emission in the stack at different significance levels, for each of the assumed initial FWHM of the broad component (800, 900, 1000, 1100, 1200 km s^{-1}). We find that for initial broad components with $\text{FWHM} > 900 \text{ km s}^{-1}$, we can retrieve excess emission of $> 1\sigma$, while we can retrieve a $> 2\sigma$ signal only for initial broad components with $\text{FWHM} > 1100 \text{ km s}^{-1}$ $\sim 27\text{--}50\%$ of the time. Example spectra from this test are shown in Fig. A.4.

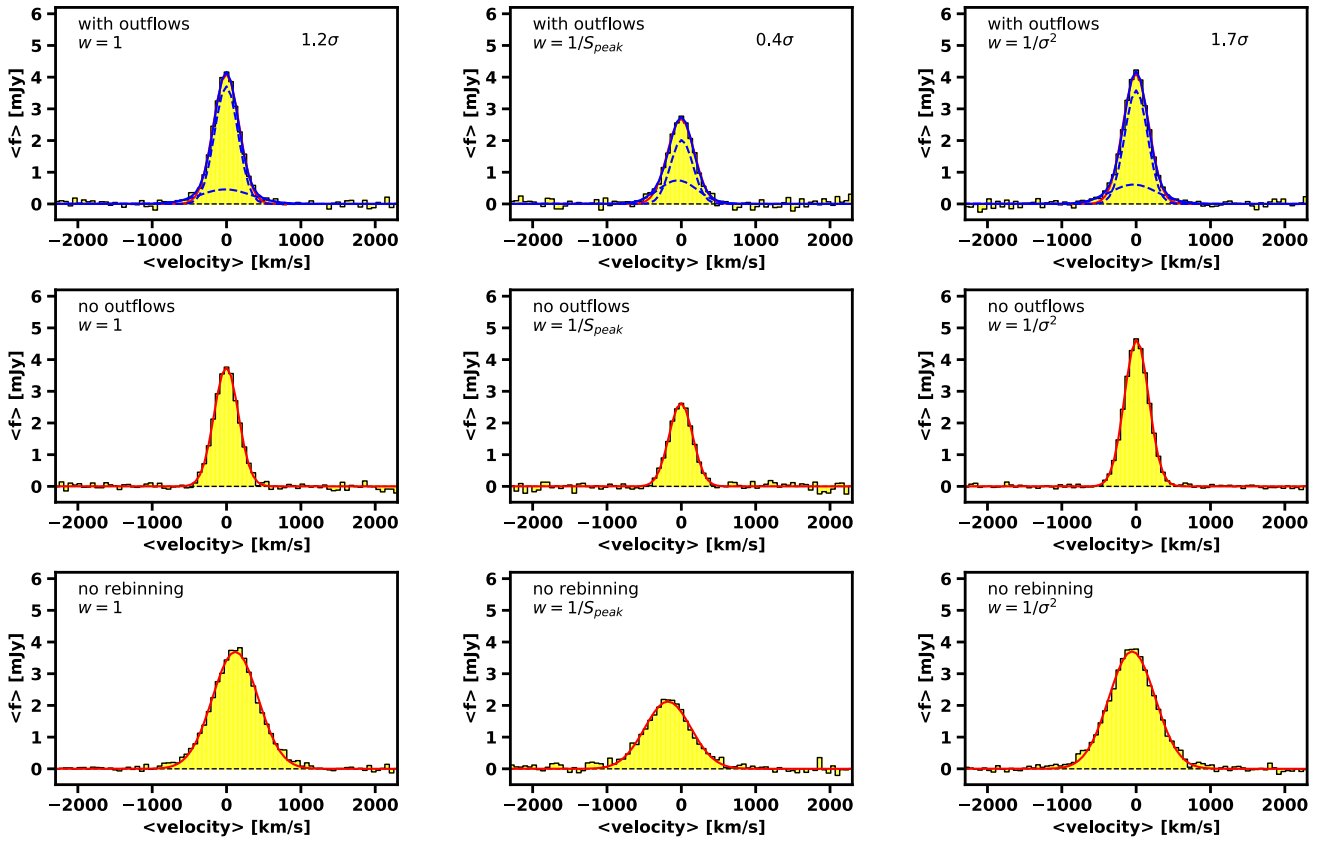


Fig. A.3: (*top*) Example spectra from the test on stacking mock samples where all sources had a broad component below the noise levels, for each of the different weights used. Also given are the significance values of the excess emission due to a broad component, for each example. (*middle*) Example spectra from the test on stacking mock samples where all sources had no added broad component. (*bottom*) Example spectra from the test on stacking mock samples where all sources had no added broad component, but without using velocity re-binning. We also show the one (red curve) and two-component fits (blue solid and dashed curves) to the stacked lines.

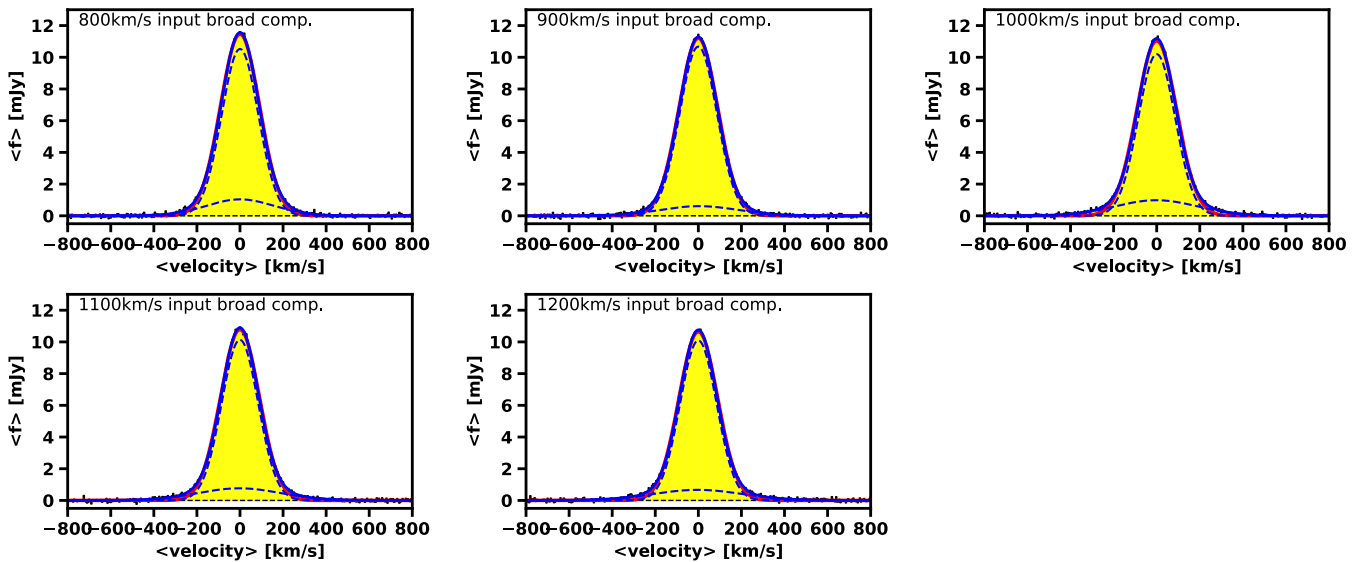


Fig. A.4: Example spectra from the orientation test, for each of the different initial broad component FWHM values. We also show the one (red curve) and two-component fits (blue solid and dashed curves) to the stacked lines.